



PCCP

[Fe₄S₄] cubane in sulfite reductases: new insights into bonding properties and reactivity

Journal:	<i>Physical Chemistry Chemical Physics</i>
Manuscript ID	CP-ART-05-2022-002124.R1
Article Type:	Paper
Date Submitted by the Author:	19-Jul-2022
Complete List of Authors:	Khan, Shahriar Noor; Auburn University, Chemistry & Biochemistry Griffith, Alexa; Oak Ridge National Laboratory De Proft, Frank; Vrije Universiteit Brussel Miliordos, Evangelos; Auburn University College of Sciences and Mathematics, Chemistry and Biochemistry Havenith, Remco; Rijksuniversiteit Groningen Stratingh Institute for Chemistry; Ghent University, Chemistry Bykov, Dmytro; Oak Ridge National Laboratory, National Center for Computational Sciences Cunha, Ana; University of Antwerp, Chemistry

SCHOLARONE™
Manuscripts

[Fe₄S₄] cubane in sulfite reductases: new insights into bonding properties and reactivity

Shahriar N. Khan,^a Alexa Griffith,^b Frank De Proft^c, Evangelos Miliordos,^a Remco W.A.

Havenith,^d Dmytro Bykov,^{b*} Ana V. Cunha,^{b,c,e*}

^a*Department of Chemistry and Biochemistry, Auburn University, Auburn, AL 36849-5312, USA*

^b*Center for Computational Sciences, Oak Ridge National Laboratory, Oak Ridge, TN 37831-6373, USA*

^c*Eenheid Algemene Chemie (ALGC), Vrije Universiteit Brussel (VUB), Pleinlaan 2, 1050 Brussels, Belgium*

^d*Stratingh Institute for Chemistry and Zernike Institute for Advanced Materials, University of Groningen, Nijenborgh 4, 9747 AG Groningen, The Netherlands and Ghent Quantum Chemistry Group, Department of Chemistry, Ghent University, Krijgslaan 281 (S3), B-9000 Gent, Belgium*

^e*Department of Chemistry of the University of Antwerp, Groenenborgerlaan 171, 2020 Antwerp, Belgium*

Email: bykovd@ornl.gov; ana.cunha@uantwerpen.be

Abstract: The dissimilatory sulfite reductase enzyme has very characteristic active site where the substrate binds to an iron site, ligated by a siroheme macrocycle and a thiol directly connected to a [Fe₄S₄] cluster. This arrangement gives the enzyme remarkable efficiency in reducing sulfite and nitrite all the way to hydrogen sulfide and ammonia. For

the first time we present a theoretical study where substrate binding modalities and activation are elucidated using active site models containing proton supply side chains and the $[\text{Fe}_4\text{S}_4]$ cluster. Density functional theory (DFT) was deployed in conjunction with the energy decomposition scheme (as implemented in AMS), the quantum theory of atoms in molecules (QTAIM), and conceptual DFT (cDFT) descriptors. We quantified the role of the electrostatic interactions inside the active site created by the side chains as well as the influence of the $[\text{Fe}_4\text{S}_4]$ cluster on the substrate binding. Furthermore, using conceptual DFT results we shed light of the activation process, thus, laying foundation for further mechanistic studies.

We found that the bonding of the ligands to the iron complex is dominated by electrostatic interactions, but the presence of the $[\text{Fe}_4\text{S}_4]$ cubane leads to substantial changes in electronic interaction. The spin state of the cubane, however, affects the binding energy only marginally. The conceptual DFT results show that the presence of the $[\text{Fe}_4\text{S}_4]$ cubane affects the reactivity of the active site as it is involved in electron transfer. This is corroborated by an increase in the electrophilicity index, thus making the active site more prone to react with the ligands. The interaction energies between the ligand and the siroheme group are also increased upon the presence of the cubane group, thus, suggesting that the siroheme group is not an innocent spectator but plays an active role in the reactivity of the dSIR active site.

Introduction

Dissimilatory sulfite reductase (dSir) is an essential enzyme in sulfur-based energy metabolism, and is a part of a redox enzyme superfamily of various sulfur- and nitrogen-

reducing proteins.¹ The dSirs reduce sulfite in the terminal redox couple of a respiratory electron-transfer chain and are found in bacteria and archaea. In the process of anaerobic respiration sulfite/sulfate-reducing prokaryotes use sulfite as a terminal electron acceptor.^{2,3} The six electron reduction happens in a very characteristic active site, in which the siroheme macrocycle is covalently bonded to a thiol, complexed with $[\text{Fe}_4\text{S}_4]$ (*i.e.*, cubane), $\text{SO}_3^{2-} + 6\text{e}^- + 8\text{H}^+ \rightarrow \text{H}_2\text{S} + 3\text{H}_2\text{O}$

Figure 1.

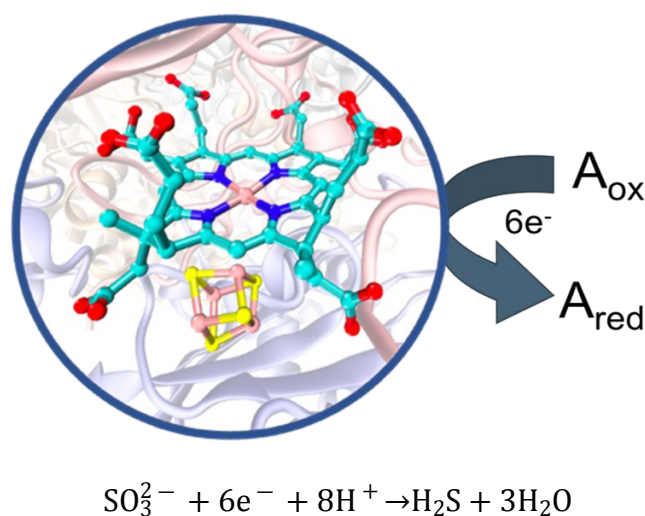


Figure 1. Schematic representation of the dSir active site.

A push-pull mechanism has been proposed wherein the pull from protonated residues couples with the push of electrons from the redox-active cofactors to the substrate, and the release of a water molecule follows cleavage of an oxygen bond on the substrate. The four active site residues, two lysines and two arginines, are essential to the active site structure, facilitating substrate binding, and are coordinating proton sources.⁴ The dSirs enzymes comprise two catalytically independent $\alpha\beta$ heterodimers with a ferredoxin domain. Each domain has one siroheme- $[\text{Fe}_4\text{S}_4]$ center, but only one of them is catalytically active.⁵⁻⁶

In the resting state of the active site, the siroheme ligates a phosphate anion that is displaced upon activation, making room for sulfite to move into the pocket and bind to the siroheme iron through sulfur.⁷ A hydrogen-bonding network consisting of water molecules, siroheme carboxylate prosthetic groups, and positively charged residues facilitates S-O bond cleavage. X-ray crystal data from Crane and co-workers show a high-spin ($S = 5$) ferric iron⁸ when bound to phosphate, and a low spin ($S = 1$) ferric iron when bound to sulfite.⁷ EPR⁸ spectra of oxidized dSir and assimilatory sulfite reductase (aSir) exhibited signals due to an $S = 5$ spin state and an $S = 2^9$ spin state. Model complex studies also show evidence of high-spin ferric hemoproteins.¹⁰

Resonance Raman spectroscopy and sulfur isotope studies suggest that an electron transfer from the $[\text{Fe}_4\text{S}_4]$ cluster facilitates the reduction of the substrates.¹¹⁻¹² Recently, Lu and co-workers successfully designed a heme- $[\text{Fe}_4\text{S}_4]$ metalloenzyme that emulates sulfite reductase.¹³ A $[\text{Fe}_4\text{S}_4]$ cluster was inserted proximal to the native heme-b center of cytochrome c peroxidase (CcP) and reached sulfite reduction activity comparable to native Sir. Both the siroheme and heme centers were able to conduct sulfite reduction, proving that siroheme is not essential for sulfite reduction.

Various spectroscopic studies have been conducted in an attempt to characterize iron-sulfur clusters in dSir enzymes. $^1\text{H-NMR}$ resonances and isomer shifts from Mössbauer spectroscopy of model complexes reveal an $[\text{Fe}_4\text{S}_4]^{2+}$ core oxidation state with an $S = 0$ ground state and a high-spin ($S = 5$) siroheme Fe(III) center.¹⁴⁻¹⁵ Mössbauer spectra of $[\text{Fe}_4\text{S}_4]^{2+}$ indicate two equivalent $\text{Fe}^{2.5+}\text{Fe}^{2.5+}$ pairs.¹⁶ Additionally, EPR studies suggest that in model complexes the ferric active site can bind with π -accepting ligands.¹⁷

Despite recent progress, there is no clear picture of Sir-substrate bonding modalities and the role of the $[\text{Fe}_4\text{S}_4]$ cluster with various substrates. The $[\text{Fe}_4\text{S}_4]^{2-}$ cluster alone has been

the subject of numerous theoretical studies (for example ¹⁸⁻²⁴). The theoretical studies prove the cluster to consist of two antiferromagnetically coupled Fe₂S₂-units, in which the two iron centers are coupled ferromagnetically. A theoretical study on the Sir intermediates where the model consisted only of heme-Fe-SO₂⁻ has been conducted and gave insight into the reduction reaction pathways.²⁵ Due to a lack of theoretical studies describing the [Fe₄S₄] cluster covalently bound to the heme and the substrates, we present a computational investigation of the Sir active site in this paper, with as goal to elucidate the effects of the [Fe₄S₄] cluster on the binding properties and electronic structure of the active site.

This study, motivated by the results of Lu et al.¹³ aims to investigate sulfite reductase binding modalities using siroheme models and to elucidate the role of the [Fe₄S₄] cluster on substrate binding and activation. We will consider the shared domain of aSir and dSir containing siroheme-[Fe₄S₄]. Nitrite and sulfite reductases (Nirs and Sirs) are structurally and functionally similar,⁹ and since the active sites of assimilatory and dissimilatory reductases are virtually identical, we consider the reduction of both sulfite and nitrite.²⁶ We therefore studied the hydrogen sulfite, sulfite, and nitrite substrates in siroheme models with and without the [Fe₄S₄] cluster. To reveal the bonding patterns and to elucidate the role of the [Fe₄S₄] cluster, we performed density functional theory (DFT) calculations on the complexes for high-, intermediate-, and low-spin states, and analyzed the bonding using the energy decomposition scheme,²⁷ the quantum theory of atoms in molecules (QTAIM),²⁸⁻²⁹ and conceptual DFT (cDFT) descriptors.³⁰⁻³¹

Computational Details

The initial structures for the active site models of the enzyme were taken from the crystal structure of the sulfite reducing archaea *Archaeoglobus fulgidus* (Protein Data Bank³² code 3MM5). The models were chosen to mimic the steric hindrance of the protein environment. Thus, the closest residues and the second sphere distal ligands were included. Also, water molecules present in the crystallographic data are expected to contribute to the reduction of the substrate via coordination with the residues; therefore, two water molecules are included in the active-site model (Figure S1). Due to the lack of parameters for metals in the current classical force fields it was not possible to perform dynamical calculations, thus the structural fluctuations of the protein were not taken into account. A more detailed description of the active site and the computational modelling can be found in section I of the Supporting Information.

The calculations were performed with the ADF program³³⁻³⁵ version 2019 using density functional theory (DFT).³⁶ The models were optimized using the BP86 functional³⁷⁻³⁸ combined with a triple- ζ Slater-type basis set (TZ2P).³⁹ The BP86 functional was chosen as a compromise between accuracy and speed, while the TZ2P is equivalent to a cc-pVTZ basis set, and geometries are usually converged with a triple- ζ basis set (distances are converged within 0.01 Å and angles by 0.3 degrees (see for example ref. ⁴⁰). Additionally, the conductor-like screening model COSMO⁴¹ ($\epsilon = 4$, to mimic the environment within a protein⁴²) and Grimme's dispersion correction⁴³ were applied to all models. Once we obtained an optimized structure, single-point calculations were performed with the TPSSh⁴⁴⁻⁴⁵ functional.

The nature of the bonding interactions in the clusters was analysed using the energy decomposition analysis (EDA) as implemented in AMS (TPSSh/TZ2P) for the high-spin, intermediate- and low-spin siroheme complexes, and high-spin cubane-siroheme

complexes. The TPSSh functional has been chosen as it demonstrates superior performance for evaluating energy differences between spin states, with a mean absolute error of only 2.6 kcal/mol for similar spin crossover complexes.⁴⁶ As we are interested in the bonding between the ligand (HSO_3^- , SO_3^{2-} , NO_2^-) and the iron active center, the fragments in these calculations were defined as a) the ligand and b) the remaining part of the Fe-cluster (referred to as the Fe-pre-complex). The cDFT calculations were also performed using ADF with the TPSSh functional and TZ2P basis set. The descriptors were calculated using the frontier molecular orbital (FMO) approximation.⁴⁷ The interaction energies between the active site and the substrates were also calculated as: $E_{\text{int}} = E_{\text{Fe-cluster}}^{\text{opt}} - [E_{\text{Fe-pre-complex}}^{\text{opt}} + E_{\text{ligand}}^{\text{opt}}]$.

Results and Discussion

The two different oxidation states of the active center namely ferrous (Fe^{2+}) and ferric (Fe^{3+}), multiple spin states (S value ranging from 0 to 5/2) are considered in this study to elucidate the binding trends of HSO_3^- , SO_3^{2-} , and NO_2^- to the active site. Selected geometric parameters (Tables S6-S7) for the optimized siroheme species (without the cubane cluster), together with the interaction energy between the substrate and the complex are presented in Table 1.

Table 1. Geometric parameters (distances (d) in Å) of the siroheme species with substrates (without the cubane cluster) optimized at BP86/TZ2P level of theory, together with substrate interaction energies (E_{int} in kcal/mol) of the species at TPSSh/TZ2P//BP86/TZ2P .

Compound	Spin State S	$d_{\text{Fe-S/N}}$	Average $d_{\text{S-O/N-O}}$	$d_{\text{S-OH}}$	E_{int}
HSO_3^-	0		1.506	1.774	
Siro- Fe^{2+} - HSO_3^-	0	2.134	1.525	1.718	-54.3
Siro- Fe^{2+} - HSO_3^-	1	2.347	1.515	1.646	-45.6
Siro- Fe^{2+} - HSO_3^-	2	2.908	1.520	1.717	-38.6
Siro- Fe^{3+} - HSO_3^-	1/2	2.329	1.536	a	-91.7
Siro- Fe^{3+} - HSO_3^-	3/2	2.809	1.553	a	-83.7
Siro- Fe^{3+} - HSO_3^-	5/2	3.016	1.518	1.702	-61.8
SO_3^{2-}	0		1.558		
Siro- Fe^{2+} - SO_3^{2-}	0	2.238	1.550		-120.7
Siro- Fe^{2+} - SO_3^{2-}	1	2.431	1.540		-104.2
Siro- Fe^{2+} - SO_3^{2-}	2	3.129	1.559		-109.7
Siro- Fe^{3+} - SO_3^{2-}	1/2	2.392	1.535		-133.8
Siro- Fe^{3+} - SO_3^{2-}	3/2	3.166	1.555		-144.8
Siro- Fe^{3+} - SO_3^{2-}	5/2	3.007	1.553		-123.2
NO_2^-	0		1.277		
Siro- Fe^{2+} - NO_2^-	0	2.396	1.312		-36.6
Siro- Fe^{2+} - NO_2^-	1	2.453	1.345		-42.5
Siro- Fe^{2+} - NO_2^-	2	2.452	1.327		-28.8
Siro- Fe^{3+} - NO_2^-	1/2	3.066	1.266		-56.9
Siro- Fe^{3+} - NO_2^-	3/2	3.182	1.268		-53.6
Siro- Fe^{3+} - NO_2^-	5/2	3.565	1.263		-54.4

^aDuring the optimization, the H-atom of HSO_3^- moved to one of the carboxylic groups of the siroheme.

For the complex with substrate HSO_3^- , the distances of the S atom from the active site iron ranges from 2.134 to 3.016 Å where the low spin state ($S = 0$) has the shortest distance compared to the intermediate and high spin state species. However, in some of the geometry optimizations, the hydrogen atom of the HSO_3^- group was transferred to one of the COO^- groups of the siroheme group. A similar trend is noticed for the complex with SO_3^{2-} as well as the low spin ($S = 0$) forms the shortest bond distance (2.238 Å) and the intermediate and high spin ($S = 3/2, 2$) have larger Fe-S distances (3.166 Å and 3.129 Å, respectively).

For the case of the complex with NO_2^- , the molecular bonding prefers the Fe^{2+} oxidation state of the active site based on $d_{\text{Fe-N}}$, and the Fe-N bond distance has a range of 2.396 to 2.453 Å (Table 1). For all spin states of the siroheme- Fe^{3+} complexed with NO_2^- , Fe-N bond distances are between 3.066 to 3.565 Å suggesting that the substrate NO_2^- is not strongly bound to the active site.

For the heme species, the substrate HSO_3^- follows a similar pattern to the siroheme species where the high spin species ($S = 2, 5/2$) have a larger Fe-S distance (3.233 Å and 3.448 Å, respectively) compared to the low spin cases and the shortest bond distance (2.176 Å) is found for the $S = 0$ spin state (Table S1). For the substrate SO_3^{2-} , the Fe-S bond distance is slightly longer than the case of the substrate HSO_3^- and the smallest bond distance is found at 2.277 Å for $S = 0$ spin state. Once again, the high spin species ($S = 2, 5/2$) have larger Fe-S bond distances (3.475 Å and 3.167 Å, respectively). However, for the substrate NO_2^- with the heme system, all the spin states from Fe^{2+} and Fe^{3+} have shorter bond distances compared to the siroheme species. The shortest bond distance is 1.824 Å that

belongs to the $S = 0$ spin state. For other spin states, the Fe-N bond distances are in the range of 1.824 to 2.052 Å.

In contrast, for the case of NO_2^- , the bare substrate has an average N-O bond distance of 1.277 Å. When NO_2^- interacts with the heme/siroheme center, a substantial elongation of the N-O bonds (ranging from 1.312 to 1.345 Å) is found. This elongation is due to the π back donation from the heme/siroheme moiety to the π orbitals of NO_2^- . Overall, an inverse correlation between Fe-N and N-O bond distances is noticeable, i.e., a shorter Fe-N distance corresponds to a longer N-O distance (Table 1 and Table S1).

The relative energies of the species and the interaction energies of the substrate with the active site were evaluated using the TPSSh functional. The full table of the relative energies is presented in the Supporting Information (Table S3). In case of siroheme TPSSh results suggest the low spin iron configuration in both oxidation states Fe^{2+} and Fe^{3+} being substantially more stable for both HSO_3^- and SO_3^{2-} substrates, in line with previous results⁷ (Table S3). The energy differences of 16.5 and 13.5 kcal/mol for HSO_3^- and 11.2 and 8.9 kcal/mol for SO_3^{2-} are predicted to separate the spin states. In case of the heme group, the situation is very different. All iron spin configurations are very close in energy (within 3 kcal/mol) except for heme- Fe^{3+} - SO_3^{2-} which is 19 kcal/mol above the ground state. The NO_2^- substrate shows the lowest energy in the intermediate spin Fe^{2+} configuration in both siroheme and heme cases. The Fe^{3+} on the contrary stays in the low-spin state for both siroheme and heme separated by 6 and 7.4 kcal/mol, respectively (Table S3). The differences in spin state energies between the heme and siroheme compounds may presumably be caused by the fact that the siroheme group is less rigid and more twisted than the heme group, hence it can lead to different ligand field splittings.

In order to gain more insight into the nature of the bonding interactions in the clusters, an energy decomposition analysis (EDA) was performed. Here, at first, we present a comprehensive discussion of the EDA analysis for the high-spin species. Then, for a comparison, EDA analyses of the low- and intermediate spin siroheme systems are provided in Table S2. The fragments in these calculations were defined as the ligand (HSO_3^- , SO_3^{2-} , NO_2^-) and the remaining part of the Fe-cluster (the Fe pre-complex). The most important components of the bonding energy, together with the bonding energy at the optimized cluster geometry and the bonding energy where relaxation of the fragments is included are listed in Table 2.

Table 2. Results of the EDA analysis (in kcal/mol) for the high-spin compounds. E_{Pauli} is the Pauli repulsion, E_{el} is the electrostatic interaction, E_{orb} is the orbital interaction, ΔE_{solv} is the difference in solvation energy between the molecule and the fragments, E_{total} is the total bonding energy at the optimized geometry of the cluster, E_{int} is the bonding energy in which the relaxation of the individual components has been taken into consideration.

Compound	E_{Pauli}	E_{el}	E_{steric}^a	E_{orb}	ΔE_{solv}	E_{total}	E_{int}
Siro-Fe ²⁺ -HSO ₃ ⁻	147.2	-263.7	-116.5	-75.0	130.3	-61.2	-38.6
Siro-Fe ³⁺ -HSO ₃ ⁻	133.6	-308.8	-175.2	-66.6	165.9	-75.9	-61.8
Siro-Fe ²⁺ -SO ₃ ²⁻	195.8	-462.3	-266.4	-132.4	267.2	-131.6	-109.7
Siro-Fe ³⁺ -SO ₃ ²⁻	197.4	-567.3	-369.9	-127.2	339.3	-157.8	-123.2
Siro-Fe ²⁺ -NO ₂ ⁻	184.5	-269.4	-84.9	-135.7	134.5	-86.1	-28.8
Siro-Fe ³⁺ -NO ₂ ⁻	75.2	-269.7	-194.5	-41.7	160.0	-76.1	-54.4

$$^a E_{\text{steric}} = E_{\text{Pauli}} + E_{\text{el}}$$

The large difference between E_{total} and E_{int} indicates that a considerable relaxation of the individual fragments takes place. The relaxation energy ranges from 69.5 kcal/mol for Siro- $\text{Fe}^{2+}\text{-NO}_2^-$ to 29.2 kcal/mol for Siro- $\text{Fe}^{3+}\text{-NO}_2^-$. For the other compounds, the relaxation energy is in the order of 40-50 kcal/mol. This relaxation is concerned with especially the rearrangement of the environment around the iron centre that has now a vacant coordination site. It is striking that in the case of ligands with a long Fe-L bond, the interaction energy between the ligand and the Fe-complex is still considerable, and in some cases even larger than the interaction between ligand and Fe-complex when the ligand is at a closer Fe-L distance.

The EDA analysis shows the different components to the bonding energy. The electrostatic component is in all cases the largest contributor: the electrostatic interaction between the negatively charged ligand and the positive charged Fe-pre-complex dominates. This is further corroborated by maps of the electrostatic potential (Figure 4), which indicate a positively charged area that can accommodate the negatively charged ligand. The total steric interaction, which is the sum of the Pauli repulsion and the electrostatic interaction, is in most cases the largest component of the total bonding energy. Only in the case of Siro- $\text{Fe}^{2+}\text{-NO}_2^-$, the orbital interaction contribution is larger. The next most important contribution is the orbital interaction contribution. A considerable polarization of the density occurs upon formation of the complex: for example, for Siro- $\text{Fe}^{2+}\text{-NO}_2^-$, electron density is pushed away from the iron center towards the cysteine sulfur atom (Figure 2 (a)). Rearrangement of the density of the ligand also occurs. The changes in the density upon formation of the complex for the Siro- Fe^{3+} structure is similar (Figure 2 (b)), although in this case a decrease of electron density at the bridging sulfur atom is found.

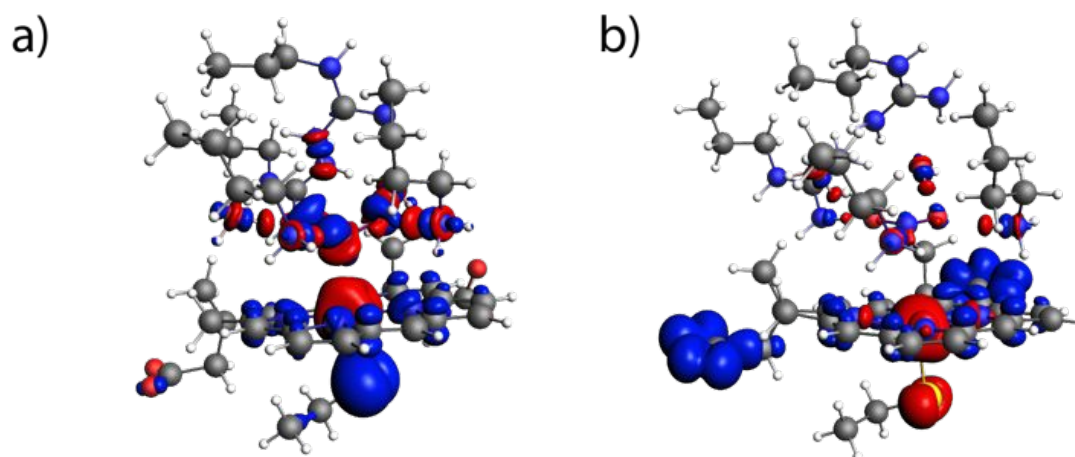


Figure 2. Density difference between the density of a) Siro-Fe²⁺-NO₂⁻ and the fragments ($\rho(\text{Siro-Fe}^{2+}\text{-NO}_2^-) - (\rho(\text{Siro-Fe}^{2+}) + \rho(\text{NO}_2^-))$) and b) Siro-Fe³⁺-NO₂⁻ and the fragments ($\rho(\text{Siro-Fe}^{3+}\text{-NO}_2^-) - (\rho(\text{Siro-Fe}^{3+}) + \rho(\text{NO}_2^-))$). Blue is positive, red negative.

The change in solvation energy is also considerable and counteracts the steric and orbital interactions. Although these cases with weakly bound ligands, the steric interaction and polarization of the electron density results in a negative bonding energy and a stabilization of the ligand when the ligand is interacting with the iron-pre-complex and its environment. The closed-shell nature of the interaction is further corroborated by the Laplacian of the density at the bond critical point between the iron atom and ligand (

Table 3). In all cases that a bond critical point was located, a positive value of the Laplacian was found, together with a low density value, indicating that the interaction between the iron atom and the ligand is mainly of closed-shell character (non-covalent).²⁸

Table 3. The density and the Laplacian of the density at the bond critical point between Fe and the ligand. N/A denotes that no bond critical point was found between Fe and the ligand.

Compound	ρ	$\nabla^2\rho$
Siro-Fe ²⁺ -HSO ₃ ⁻	0.0210	0.0572
Siro-Fe ³⁺ -HSO ₃ ⁻	0.0182	0.0452
Siro-Fe ²⁺ -SO ₃ ²⁻	0.0148	0.0370
Siro-Fe ³⁺ -SO ₃ ²⁻	0.0197	0.0449
Siro-Fe ²⁺ -NO ₂ ⁻	0.0332	0.0985
Siro-Fe ³⁺ -NO ₂ ⁻	N/A	N/A

Upon addition of the (ferromagnetic) cubane moiety, the bonding energy for some of the compounds is remarkably similar to the one obtained without the cubane (Table 4 and Table S3). However, the decomposition of the bonding energy of the different compounds reveals that all contributions are different. The orbital interaction energy is in all cases larger, while the steric interaction is smaller except for the Fe²⁺/Fe³⁺-SO₃²⁻ compounds.

Table 4. Results of the EDA analysis (all in kcal/mol) for the high-spin compounds with the cubane.

Compound	E _p	E _{el}	E ^a _{st}	E _{or}	ΔE	E _{tot}
	auli		eric	b	solv	al
Cub-Siro-Fe ²⁺ -	16	-	-	-	11	-
HSO ₃ ⁻	8.2	243.4	75.2	103.6	4.9	63.8
Cub-Siro-Fe ³⁺ -	16	-	-	-	14	-
HSO ₃ ⁻	2.1	294.1	132.0	97.9	4.5	85.4
Cub-Siro-Fe ²⁺ -	18	-	-	-	23	-

SO ₃ ²⁻	4.8	410.9	226.1	130.2	6.3	120.0
Cub-Siro-Fe ³⁺ -	19	-	-	-	27	-
SO ₃ ²⁻	0.7	488.1	297.4	115.5	4.5	138.4
Cub-Siro-Fe ²⁺ -	17	-	-	-	13	-
NO ₂ ⁻	6.2	244.9	68.7	170.5	5.9	103.2
Cub-Siro-Fe ³⁺ -	18	-	-	-	16	-
NO ₂ ⁻	3.9	301.5	117.6	139.1	4.7	92.0

$${}^a E_{\text{steric}} = E_{\text{Pauli}} + E_{\text{el}}$$

Changes in the density upon formation of the complex are depicted in Figure 3 (and Figure S3). As in the siroheme case, upon complex formation, the density at the central Fe-atom decreases and is pushed towards the sulfur atom attached to it. However, further shifts of the density at the cubane moiety occurs, indicating that the cubane moiety is not unaffected by the formation of the bond. Furthermore, the density and the Laplacian of the density at the bond critical point between the Fe atom and the ligand (

Table 5) indicate that, just like in the case of the siroheme compounds, the bond is of closed-shell nature.

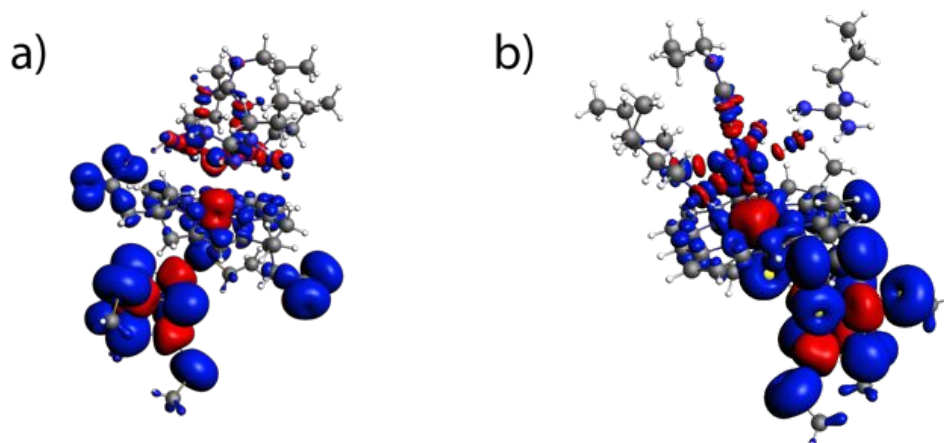


Figure 3. Density difference between the density of a) Cub-Siro-Fe²⁺-NO₂⁻ and the fragments ($\rho(\text{Cub-Siro-Fe}^{2+}\text{-NO}_2^-)-(\rho(\text{Cub-Siro-Fe}^{2+})+\rho(\text{NO}_2^-))$), and b) Cub-Siro-Fe³⁺-NO₂⁻ and the fragments ($\rho(\text{Cub-Siro-Fe}^{3+}\text{-NO}_2^-)-(\rho(\text{Cub-Siro-Fe}^{3+})+\rho(\text{NO}_2^-))$). Blue is positive, red negative.

Table 5. The density and the Laplacian of the density at the bond critical point between Fe and the ligand. N/A denotes that no bond critical point was found between Fe and the ligand.

Compound	ρ	$\nabla^2\rho$
Cub-Siro-Fe ²⁺ -	0.0	0.0
HSO ₃ ⁻	181	496
Cub-Siro-Fe ³⁺ -	N/	N/
HSO ₃ ⁻	A	A
Cub-Siro-Fe ²⁺ -	0.0	0.0
SO ₃ ²⁻	196	506
Cub-Siro-Fe ³⁺ -	0.0	0.0
SO ₃ ²⁻	311	774
Cub-Siro-Fe ²⁺ -	0.0	0.0
NO ₂ ⁻	167	455
Cub-Siro-Fe ³⁺ -	0.0	0.1
NO ₂ ⁻	514	636

As mentioned before, the interaction between the ligand and the Fe-pre-complexes is mainly of closed-shell nature (non-covalent), and strong bonding energies are found, even though in some cases the Fe-ligand bond is rather long. Maps of the electrostatic potential

(Figure 4, and Figures S6, S7) show that the negatively charged ligand is positioned in a positively charged environment. This positively charged environment is created by the positively charged amino acids forming the cavity and the iron atom. Little differences are observed between the cavity formed for the siroheme and the cubane-siroheme complexes. This explains the strong interactions between the ligand and the pre-complex, and that the bonding energies between the siroheme and cubane-siroheme complexes are very similar.

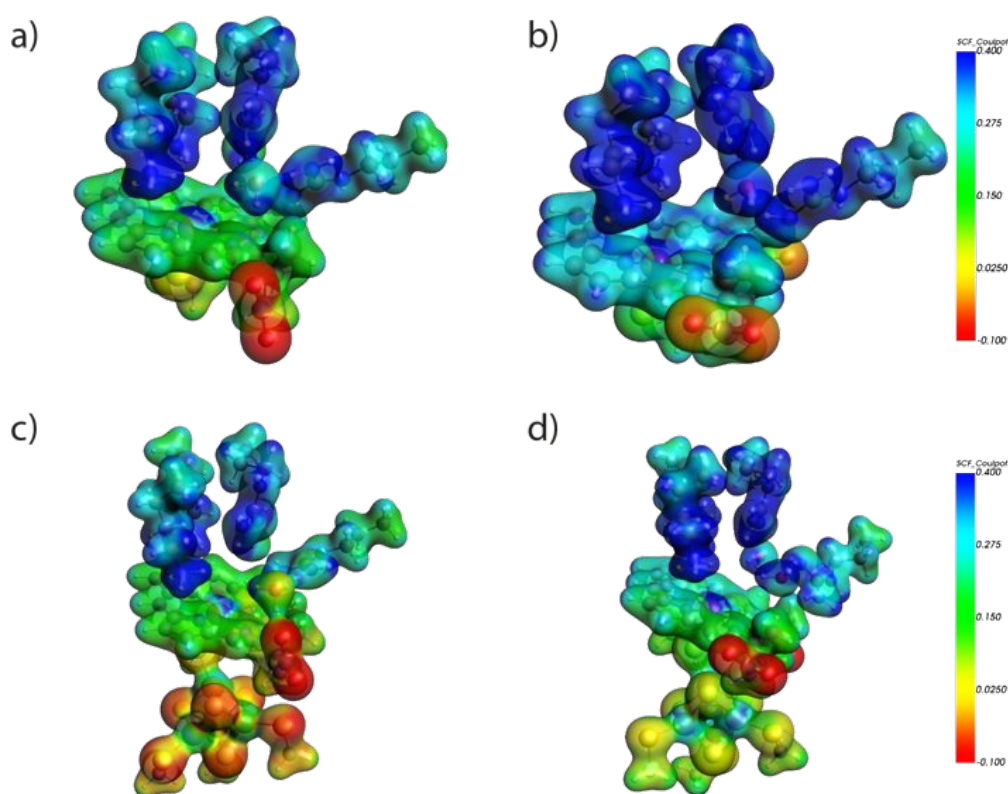


Figure 4. Maps of the electrostatic potential, plotted at a density isosurface (isovalue 0.03) for the pre-complexes.

Further insight into the chemistry of these complexes is provided by conceptual DFT. Isosurface plots of the dual descriptor for the pre-complexes of the $\text{Fe}^{2+/3+}-(\text{SO}_3^{2-})$ siroheme and cubane-siroheme compounds within the frontier molecular orbital (FMO) approach are

shown in Figure 5, and selected cDFT descriptors are listed in Table 6 (full list of plots, Figures S4, S5, and cDFT descriptors Table S4). Comparison of the plots of the dual descriptor for the three consecutive pre-complexes differ significantly, i.e., the plots differ for the pre-complexes of Siro-Fe²⁺-(L), Siro-Fe³⁺-(L), Cub-Siro-Fe²⁺-(L), and Cub-Siro-Fe³⁺-(L), while these pre-complexes are the same for the different L ligands. This variation is also discernible in the cDFT descriptors. However, as the geometry of the pre-complex is taken from the optimized geometry of the complex with the ligand, the differences in the geometry of the parent compound (Cub-)Siro-Feⁿ⁺-(L) and the embedding environment are responsible for these differences between the pre-complexes. It should be mentioned that the variations due to changes in the environment and geometry are larger than changes due to the addition of the cubane. The global descriptors do show some trend upon the addition of the cubane moiety: the hardness decreases slightly, and concomitantly the softness increases, and the electrophilicity index increases, except for the Fe²⁺-SO₃²⁻ complex, where it remains virtually the same. This trend is more pronounced for the Fe³⁺ complexes, and upon oxidation the electrophilicity index increases further, indicating the larger electron deficiency of the oxidised species. Other changes are minor, and not chemically significant.

The local descriptors are more difficult to interpret, and are more influenced by the geometry and environment than by the absence or presence of the cubane moiety. This is likely caused by the fact that in the FMO approach, the local descriptors are dependent on the HOMO and LUMO of the complex, and the HOMO is one of the singly occupied d-orbitals, from the manifold of singly occupied d-orbitals.

The ligands in all three cases are negatively charged ions, thus they behave like nucleophiles, and are expected to bind to the electrophilic regions of the pre-complex (indicated in blue in Figure 5). However, the dual descriptor plots (Figure 5) are not so

straightforward to interpret for the same reason as for the local descriptors. For the Siro- Fe^{2+} - (SO_3^{2-}) and Siro- Fe^{2+} - (NO_2^-) pre-complexes, an electrophilic region above the iron atom is created by the (positively charged) environment. Upon oxidation to Fe^{3+} , the iron center itself becomes electrophilic, indicating that the negatively charged ligand can favourably interact with the complex.

Table 6. Selected cDFT descriptors for the $\text{Fe}^{2+/3+}$ - (SO_3^{2-}) pre-complex, the Cub- $\text{Fe}^{2+/3+}$ - (SO_3^{2-}) pre-complex, and the ligands.

	Siro- Fe^{2+} - (SO_3^{2-})	Cub-Siro- Fe^{2+} - (SO_3^{2-})	Siro- Fe^{3+} - (SO_3^{2-})	Cub-Siro- Fe^{3+} - (SO_3^{2-})
Hardness	0.042	0.044	0.053	0.026
Softness	23.792	22.681	18.769	38.799
Electrophilicity index	0.236	0.216	0.380	0.630
$f^+(\text{Fe})$	0.116	0.003	0.556	0.057
$f(\text{Fe})$	0.656	0.160	0.002	0.631
$f^0(\text{Fe})$	0.386	0.082	0.279	0.344
$f^{(2)}(\text{Fe})$	-0.540	-0.157	0.554	-0.575
Mul. ch. (Fe)	0.746	0.754	0.811	0.764
Spin pop (Fe)	3.741	3.779	4.023	3.821
	HSO_3^{2-}	SO_3^{2-}	NO_2^-	
Hardness	0.229	0.260	0.156	
Softness	4.376	3.850	6.424	
Electrophilicity index	0.007	0.006	0.012	

$f^+(L)$	0.249	0.393	0.500
$f^-(L)$	0.337	0.364	0.346
$f^0(L)$	0.293	0.378	0.423
$f^{(2)}(L)$	-0.088	0.029	0.155

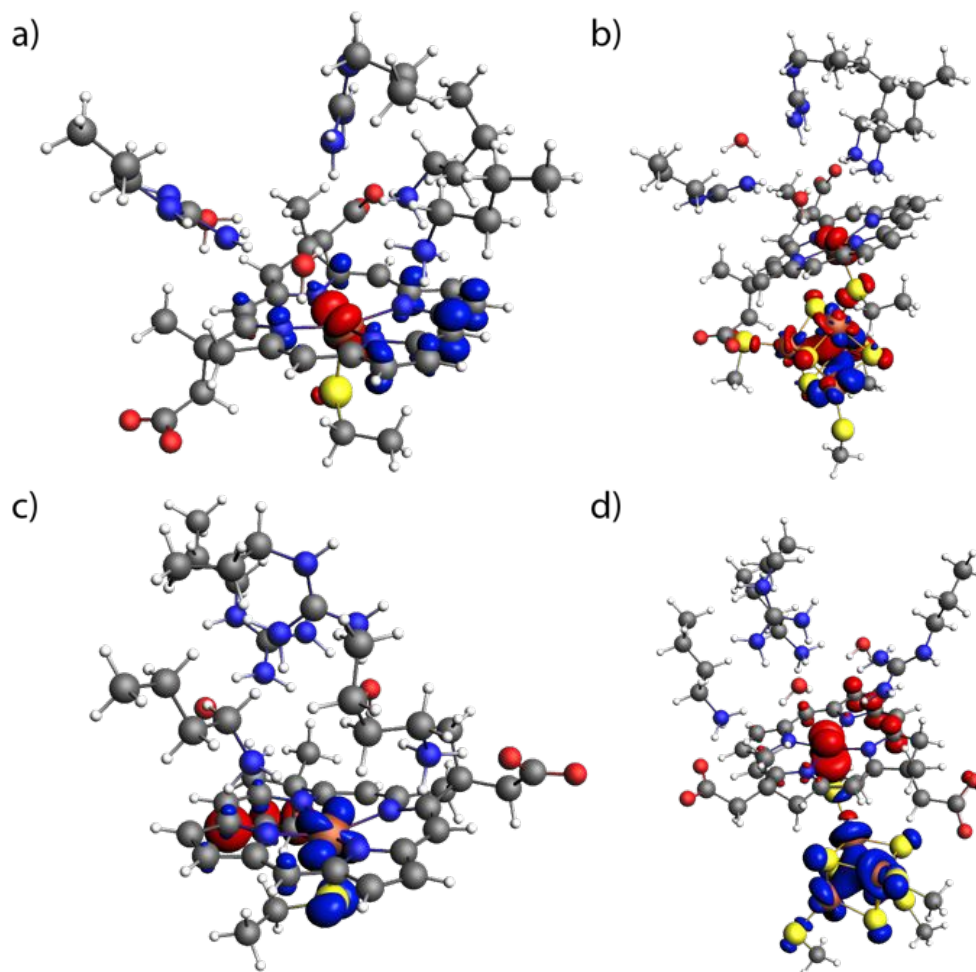


Figure 5. Isosurface plots of the dual descriptor of the pre-complexes, using the FMO approximation, of a) Siro-Fe²⁺-(SO₃²⁻), b) Cub-Siro-Fe²⁺-(SO₃²⁻), c) Siro-Fe³⁺-(SO₃²⁻), d) Cub-Siro-Fe³⁺-(SO₃²⁻) pre-complexes. Blue is positive (electrophilic regions), red negative (nucleophilic regions).

When the cubane is attached to the complex, the picture changes: the cubane is involved in the dual descriptor, and provides areas for both electrophilic and nucleophilic attack. The iron atom is in most cases neither electrophilic nor nucleophilic. In the Cub-Siro-Fe²⁺-(NO₂⁻) pre-complex, the side chains create a more nucleophilic environment, whereas the iron atom is electrophilic. In the Cub-Siro-Fe³⁺-(L) pre-complexes, the iron atom is (slightly) nucleophilic, which is indicative for the HOMO being localized on the iron (d-) orbitals.

The trend in bonding is better explained by the descriptors of the ligands. The softness of the NO₂⁻ ligand is the largest, and for this ligand, the bond, although dominated by electrostatic interactions, has the largest orbital interaction energy, suggesting that this bond may have some covalent character.

Thus, upon addition of the cubane moiety, the interaction energy between the ligand and the pre-complex increases, and concomitantly, the electrophilicity index is increased. The interaction between the ligand and the iron center is mainly ionic, but upon binding of the ligand, shifts in electron density are still observable in the cubane moiety, indicating that this moiety can play a role in transferring electrons from and to the reduction site.

Table 7. Selected cDFT descriptors for the Fe^{2+/3+}-SO₃²⁻ complex, and the Cub-Fe^{2+/3+}-SO₃²⁻ complex.

	Siro-Fe²⁺-	Cub-Siro-	Siro-Fe³⁺-	Cub-Siro-Fe³⁺-
	SO₃²⁻	Fe²⁺-SO₃²⁻	SO₃²⁻	SO₃²⁻
Hardness	0.042	0.027	0.057	0.022
Softness	23.746	36.423	17.691	45.208
Electrophilicity index	0.100	0.195	0.212	0.467

$f^+(\text{Fe})$	0.121	0.005	0.623	0.355
$f^-(\text{Fe})$	0.661	0.668	0.028	0.338
$f^0(\text{Fe})$	0.391	0.336	0.325	0.347
$f^{(2)}(\text{Fe})$	-0.541	-0.663	0.595	0.017
Mul. ch. (Fe)	0.710	0.703	0.712	0.672
Spin pop (Fe)	3.759	3.793	4.054	3.993

As the complex can react further in the catalytic cycle, the cDFT descriptors for the final complexes are reported and they show similar, but more pronounced, trends (

Table 7 and Table S5): the softness and the electrophilicity index increases upon addition of the cubane moiety, and both increase upon oxidation. No clear trends in the local descriptors are discernible. Furthermore, the electrophilicity index of these complexes is smaller than that of the pre-complexes, because the complexation has taken place.

Finally, the effect of the spin state of the cubane moiety on the cDFT descriptors and the binding energy has been studied. It is known from literature¹⁴⁻¹⁵ that the iron centers in the cubane moiety are antiferromagnetically coupled. We therefore performed the energy decomposition analysis also for the Cub-Siro-Fe^{2+/3+}-SO₃²⁻ compounds, together with a calculation of the cDFT descriptors. The cDFT descriptors were calculated for the six different possibilities of the spin distribution in the pre-complex, and the EDA was performed for the lowest energy configuration (Table 8). The binding energies for both the Fe²⁺ and Fe³⁺ complex with an antiferromagnetically coupled cubane moiety, are very similar to those obtained with a ferromagnetically coupled cubane system. The spin state of the cubane clearly does not play an important role here. However, the global cDFT descriptors for the Fe³⁺ pre-complex change, in particular the softness increases and the electrophilicity

index. The local descriptors only marginally change in this case, in contrast to the Fe^{2+} pre-complex, where the global descriptors are similar, and the local descriptors change. For the final Fe^{2+} complex, the global descriptors change and a decrease in the softness is discernible, together with a decrease of the electrophilicity index. The local descriptors are remarkably similar in this case. For the final Fe^{3+} complex, the softness is considerably larger, and so is the electrophilicity index. The local descriptors also changed considerably. These changes in cDFT descriptors are most likely caused by the fact that they were evaluated using the FMO approach, thus, they are derived from the frontier molecular orbitals and their energies. As there are many, nearly degenerate, orbitals around the HOMO-LUMO gap, relatively small changes in orbital energies can change the cDFT descriptors significantly. The large changes in descriptors in this case most likely do not correspond to large changes in reactivity.

Table 8. The energy decomposition analysis and cDFT descriptors for the Cub-Siro- $\text{Fe}^{2+/3+}$ - (SO_3^{2-}) pre-complexes, and the Cub-Siro- $\text{Fe}^{2+/3+}$ - SO_3^{2-} complexes.

	Cub-Siro- Fe^{2+} - (SO_3^{2-})	Cub-Siro- Fe^{3+} - (SO_3^{2-})	Cub-Siro- Fe^{2+} - SO_3^{2-}	Cub-Siro- Fe^{3+} - SO_3^{2-}
Spin distribution	$\alpha\beta\beta\alpha$	$\alpha\beta\beta\alpha$	$\alpha\beta\beta\alpha$	$\alpha\beta\beta\alpha$
E_{Pauli}			184.6	190.6
E_{el}			-413.6	-484.5
$E_{\text{steric}}^{\text{a}}$			-229.0	-293.9
E_{orb}			-129.3	-123.8
ΔE_{solv}			237.6	283.2

E_{total}			-120.8	-134.5
Hardness	0.046	0.033	0.055	0.011
Softness	21.548	30.501	18.039	88.475
Electrophilicity index	0.193	0.451	0.074	0.795
$f^+(\text{Fe})$	0.104	0.000	0.110	0.015
$f(\text{Fe})$	0.001	0.651	0.685	0.662
$f^0(\text{Fe})$	0.052	0.326	0.397	0.338
$f^{(2)}(\text{Fe})$	0.102	-0.651	-0.575	-0.647
Mul. ch. (Fe)	0.746	0.746	0.692	0.631
Spin pop (Fe)	3.732	3.729	3.733	3.717

Conclusions

In this study we explain in detail the interaction of the substrates with the active site in dSir. Our EDA analysis for the models without the $[\text{Fe}_4\text{S}_4]$ cubane showed that the electrostatic component in all cases is the largest contributor. However, upon the addition of the $[\text{Fe}_4\text{S}_4]$ cubane the decomposition of the bonding energy of the different compounds changes: the orbital interaction energy is in all cases larger, while the steric interaction is smaller except for the $\text{Fe}^{2+}/\text{Fe}^{3+}\text{-SO}_3^{2-}$ compounds. The bond critical point analysis revealed, that upon substrate complex formation, the density at the central Fe-atom decreases as well as the density at the cubane moiety is pushed towards the sulfur atom attached to it. The density and the Laplacian of the density at the bond critical point between the Fe atom and the ligand indicate that the bond is of closed-shell nature. Thus, our results suggest that for

dSirs substrate binding electrostatics plays a major role, but the presence of the [Fe₄S₄] cubane leads to substantial changes in electronic interaction.

Furthermore, conceptual DFT results show that the presence of the [Fe₄S₄] cubane affects the reactivity of the active site as it is involved in electron transfer. This is corroborated by an increase in the electrophilicity index, thus making the active site more prone to react with the ligands. The interaction energies between the ligand and the siroheme group are also increased upon the presence of the cubane group, thus, suggesting that the siroheme group is not an innocent spectator but plays an active role in the reactivity of the dSIR active site. The bonding of the ligands to the iron complex is dominated by electrostatic interactions, and the spin state of the cubane affects the binding energy only marginally. Upon addition of the cubane moiety, the interaction energy between the ligand and the pre-complex increases, and concomitantly, the electrophilicity index is increased.

Author contributions

All authors contributed equally to this paper.

Conflict of Interests

There are no conflicts to declare.

Acknowledgments

This work was sponsored by NWO Exact and Natural Sciences for the use of supercomputer facilities (EINF-431 and contract no. 17197 7095). RWAH and A. V. Cunha thank S. Dolas (SURF, NL) for allowing us to perform calculations on the experimental AMD platform

kleurplaat maintained and operated by SURF Open Innovation Lab. This research used resources of the Oak Ridge Leadership Computing Facility, which is a DOE Office of Science User Facility supported under Contract DE-AC05-00OR22725.

Supporting Information

Computational information, together with Table S1, containing the geometric parameters of the heme species with substrates, Table S2, containing the results of the EDA analysis for the low and intermediate-spin siroheme-compounds, Table S3, containing the results of the EDA analysis for the high-spin compounds, and Table S4, containing the density and the Laplacian of the density at the bond critical point between Fe and the ligand.

References

1. Oliveira, T. F.; Franklin, E.; Afonso, J.; Oldham, N.; Pereira, I. A. C.; Archer, M., Structural insights into dissimilatory sulfite reductases: Structure of desulforubidin from *desulfomicrobium norvegicum*. *Front. Microbiol.* **2011**, *2*, 71.
2. Oliveira, T. F.; Vonrhein, C.; Matias, P. M.; Venceslau, S. S.; Pereira, I. A. C.; Archer, M., The crystal structure of *desulfovibrio vulgaris* dissimilatory sulfite reductase bound to dsrC provides novel insights into the mechanism of sulfate respiration. *J. Biol. Chem.* **2008**, *283*, 34141-34149.
3. Parey, K.; Warkentin, E.; Kroneck, P. M. H.; Ermler, U., Reaction cycle of the dissimilatory sulfite reductase from *archaeoglobus fulgidus*. *Biochemistry* **2010**, *49*, 8912-8921.

4. Smith, W.; Stroupe, M. E., Mutational analysis of sulfite reductase hemoprotein reveals the mechanism for coordinated electron and proton transfer. *Biochemistry* **2012**, *51*, 9857-9868.
5. Loy, A.; Duller, S.; Wagner, M., Evolution and ecology of microbes dissimilating sulfur compounds: Insights from siroheme sulfite reductases. In *Microbial Sulfur Metabolism*, Dahl, C.; Friedrich, C. G., Eds. Springer Berlin Heidelberg, Berlin, Heidelberg: 2008; pp 46-59.
6. Schiffer, A.; Parey, K.; Warkentin, E.; Diederichs, K.; Huber, H.; Stetter, K. O.; Kroneck, P. M. H.; Ermler, U., Structure of the dissimilatory sulfite reductase from the hyperthermophilic archaeon *archaeoglobus fulgidus*. *J. Mol. Biol.* **2008**, *379*, 1063-1074.
7. Crane, B. R.; Siegel, L. M.; Getzoff, E. D., Sulfite reductase structure at 1.6 Å: Evolution and catalysis for reduction of inorganic anions. *Science* **1995**, *270*, 59-67.
8. Wagner, M.; Roger, A. J.; Flax, J. L.; Brusseau, G. A.; Stahl, D. A., Phylogeny of dissimilatory sulfite reductases supports an early origin of sulfate respiration. *J. Bacteriol. Res.* **1998**, *180*, 2975-2982.
9. Swamy, U.; Wang, M.; Tripathy, J. N.; Kim, S.-K.; Hirasawa, M.; Knaff, D. B.; Allen, J. P., Structure of spinach nitrite reductase: Implications for multi-electron reactions by the iron-sulfur:siroheme cofactor. *Biochemistry* **2005**, *44*, 16054-16063.
10. Scheidt, W. R.; Cohen, I. A.; Kastner, M. E., A structural model for heme in high-spin ferric hemoproteins. iron atom centering, porphyrin core expansion, and molecular stereochemistry of high-spin diaquo(meso-tetraphenylporphyrinato)iron(III) perchlorate. *Biochemistry* **1979**, *18*, 3546-3552.

11. Han, S.; Madden, J. F.; Siegel, L. M.; Spiro, T. G., Resonance raman studies of escherichia coli sulfite reductase hemoprotein. 3. bound ligand vibrational modes. *Biochemistry* **1989**, *28*, 5477-5485.
12. Leavitt, W. D.; Bradley, A. S.; Santos, A. A.; Pereira, I. A. C.; Johnston, D. T., Sulfur isotope effects of dissimilatory sulfite reductase. *Front. Microbiol.* **2015**, *6*, 1392.
13. Mirts, E. N.; Petrik, I. D.; Hosseinzadeh, P.; Nilges, M. J.; Lu, Y., A designed heme-[4Fe-4S] metalloenzyme catalyzes sulfite reduction like the native enzyme. *Science* **2018**, *361*, 1098-1101.
14. Cai, L.; Holm, R. H., Synthesis and electron delocalization of [fe₄s₄]-s-fe(iii) bridged assemblies related to the exchange-coupled catalytic site of sulfite reductases. *J. Am. Chem. Soc.* **1994**, *116*, 7177-7188.
15. Zhou, C.; Cai, L.; Holm, R. H., Synthesis of a [fe₄s₄]sferriheme bridged assembly containing an isobacteriochlorin component: A further analogue of the active site of sulfite reductase. *Inorg. Chem.* **1996**, *35*, 2767-2772.
16. Beinert, H.; Holm, R. H.; Münck, E., Iron-sulfur clusters: Nature's modular, multipurpose structures. *Science* **1997**, *277*, 653-659.
17. Tan, J.; Cowan, J. A., Enzymic redox chemistry: a proposed reaction pathway for the six-electron reduction of sulfite to sulfide by the assimilatory-type sulfite reductase from *desulfovibrio vulgaris* (hildenborough). *Biochemistry* **1991**, *30*, 8910-8917.
18. Bergeler, M.; Stiebritz, M. T.; Reiher, M., Structure-Property Relationships of Fe₄S₄ Clusters. *ChemPlusChem* **2013**, *78*, 1082-1098.
19. Wang, X.-B.; Niu, S.; X., Y.; Ibrahim, S. K.; Pickett, C. J.; Ichiye, T.; Wang, L.-S., Probing the Intrinsic Electronic Structure of the Cubane [4Fe-4S] Cluster: Nature's Favorite Cluster for Electron Transfer and Storage. *J. Am. Chem. Soc.* **2003**, *125*, 14072-14081.

20. Geurts, P. J. M.; Gosselink, J. W.; Van der Avoird, A.; Baerends, E. J.; Snijders, J. G., Hartree-Fock-Slater-LCAO calculations on $[\text{Fe}_4\text{S}_4(\text{SH})_4]^{0,2-,3-}$: A model for the 4-Fe active site in high potential iron protein and ferredoxin. *Chem. Phys.* **1980**, *46*, 133-148.
21. Greco, C.; Fantucci, P.; Ryde, U.; De Gioia, L., Fast Generation of Broken-Symmetry States in a Large System including Multiple Iron-Sulfur Assemblies: Investigation of QM/MM Energies, Clusters Charges and Spin Populations. *Int. J. Quantum Chem.* **2011**, *111*, 3949-3960.
22. Chen, S.-L.; Siegbahn, P. E. M., Insights into the Chemical Reactivity in Acetyl-CoA Synthase. *Inorg. Chem.* **2020**, *59*, 15167-15179.
23. Elghobashi-Meinhardt, N.; Tombolelli, D.; Mroginski, M. A., Electronic and Structural Properties of the Double Cubane Iron-Sulfur Cluster. *Catalysts* **2021**, *11*, 245.
24. Torres, R. A.; Lovell, T.; Noodleman, L.; Case, D. A., Density Functional and Reduction Potential Calculations of Fe_4S_4 Clusters. *J. Am. Chem. Soc.* **2003**, *125*, 1923-1936.
25. Surducun, M.; Brânzanic, A. M.; Silaghi-Dumitrescu, R., Heme fe-so₂ intermediates in sulfite reduction: Contrasts with fe-oo₂ species from oxygen–oxygen bond activating systems. *Int. J. Quantum Chem.* **2018**, *118*, e25697.
26. Gerlach, D. L.; Coucouvanis, D.; Lehnert, N., Connecting [4fe–4s] clusters and hemes – towards modeling the active site of sulfite reductase. *Eur. J. Inorg. Chem.* **2013**, *2013*, 3883-3890.
27. Bickelhaupt, M. F.; Baerends, E. J., Density Functional Theory: Predicting and Understanding Chemistry. In *Rev. Comput. Chem.*, Lipkowitz, K. B.; Boyd, D. B., Eds. Wiley-VCH: New York: 2000; Vol. 15, pp 1-86.
28. Bader, R. F. W., A quantum theory of molecular structure and its applications. *Chem. Rev.* **1991**, *91*, 893-928.

29. Bader, R. F. W., *Atoms in Molecules*. Clarendon Press: 1994.
30. Geerlings, P.; Chamorro, E.; Kumar Chattaraj, P.; De Proft, F.; Gázquez, J. L.; Liu, S.; Morell, C.; Toro-Labbé, A.; Vela, A.; Ayers, P., Conceptual density functional theory: status, prospects, issues. *Theoret. Chem. Acc.* **2020**, *139*, 36.
31. Geerlings, P.; De Proft, F.; Langenaecker, W., Conceptual Density Functional Theory. *Chem. Rev.* **2003**, *103*, 1793-1874.
32. Berman, H. M.; Westbrook, J.; Feng, Z.; Gilliland, G.; Bhat, T. N.; Weissig, H.; Shindyalov, I. N.; Bourne, P. E., The protein data bank. *Nucleic Acids Res.* **2000**, *28*, 235-242.
33. te Velde, G.; Bickelhaupt, F. M.; Baerends, E. J.; Fonseca Guerra, C.; van Gisbergen, S. J. A.; Snijders, J. G.; Ziegler, T., Chemistry with ADF. *J. Comput. Chem.* **2001**, *22* (9), 931-967.
34. Baerends, E. J. *ADF2019.01, SCM, Theoretical Chemistry, Vrije Universiteit, Amsterdam, The Netherlands, <http://www.scm.com>, 2019.*
35. Fonseca Guerra, C.; Snijders, J. G.; te Velde, G.; Baerends, E. J., Towards an order-N DFT method. *Theor. Chem. Acc.* **1998**, *99*, 391-403.
36. Neese, F., A critical evaluation of DFT, including time-dependent DFT, applied to bioinorganic chemistry. *J. Biol. Inorg. Chem.* **2006**, *11* (6), 702-711.
37. Becke, A. D., Density functional calculations of molecular bond energies. *J. Chem. Phys.* **1986**, *84* (8), 4524-4529.
38. Perdew, J. P., Density-functional approximation for the correlation energy of the inhomogeneous electron gas. *Phys. Rev. B* **1986**, *33* (12), 8822-8824.
39. Van Lenthe, E.; Baerends, E. J., Optimized Slater-type basis sets for the elements 1–118. *J. Comput. Chem.* **2003**, *24* (9), 1142-1156.

40. Miliordos, E.; Xantheas, S. S., On the validity of the basis set superposition error and complete basis set limit extrapolations for the binding energy of the formic acid dimer. *J. Chem. Phys.* **2015**, *142*, 094311.
41. Pye, C. C.; Ziegler, T., An implementation of the conductor-like screening model of solvation within the Amsterdam density functional package. *Theoret. Chem. Acc.* **1999**, *101* (6), 396-408.
42. Li, L.; Li, C.; Zhang, Z.; Alexov, E., On the Dielectric “Constant” of Proteins: Smooth Dielectric Function for Macromolecular Modeling and Its Implementation in DelPhi. *J. Chem. Theory Comput.* **2013**, *9*, 2126-2136.
43. Grimme, S.; Antony, J.; Ehrlich, S.; Krieg, H., A consistent and accurate ab initio parametrization of density functional dispersion correction (DFT-D) for the 94 elements H-Pu. *J. Chem. Phys.* **2010**, *132* (15), 154104.
44. Tao, J.; Perdew, J. P.; Staroverov, V. N.; Scuseria, G. E., Climbing the Density Functional Ladder: Nonempirical MetaGeneralized Gradient Approximation Designed for Molecules and Solids. *Phys. Rev. Lett.* **2003**, *91*, 146401.
45. Staroverov, V. N.; Scuseria, G. E.; Tao, J.; Perdew, J. P., Comparative assessment of a new nonempirical density functional: Molecules and hydrogen-bonded complexes. *J. Chem. Phys.* **2003**, *119*, 12129-12137.
46. Jensen, K. P.; Cirera, J., Accurate Computed Enthalpies of Spin Crossover in Iron and Cobalt Complexes. *J. Phys. Chem. A* **2009**, *113*, 10033-10039.
47. Hoffmann, G.; Tognetti, V.; Joubert, L., Can molecular and atomic descriptors predict the electrophilicity of Michael acceptors? *J. Mol. Model.* **2018**, *24*, 281.